Title: Sintering mechanics of binder jet 3D printed ceramics treated with a reactive binder

Authors: Lynnora O. Grant[1], C. Fred Higgs III[2], Zachary C. Cordero[3]

Affiliation:

1. Materials Science and NanoEngineering, Rice University, Houston, TX 77005
2. Mechanical Engineering, Rice University, Houston, TX 77005
3. Aeronautics and Astronautics, Massachusetts Institute of Technology, Cambridge, MA 02139

Corresponding author: Zachary Cordero; zcordero@mit.edu; 617-253-8821

Abstract: Reactive binders mitigate distortion during sintering of binder jet 3D printed components by precipitating a solid phase that reinforces interparticle contacts. The present work combines experiments with micromechanical modeling to clarify how aqueous titanium bis-ammonium lactato dihydroxide (TALH), a reactive binder, affects creep and densification during sintering of binder jet printed TiO_2. TALH treatment of as-printed material results in a nanocrystalline TiO_2 overlayer that coats the micron-scale particles. At sintering temperatures, this overlayer is consumed via grain growth such that the structures of the TALH-treated and neat materials appear nearly identical. Creep rates are slower in the TALH-treated material than in the as-printed TiO_2, but creep in the treated material is faster when compared at equivalent relative density. TALH-treated and neat TiO_2 both exhibit diffusional creep, with stress exponents near unity and activation energies of ~400 kJ/mol. Models of structural evolution in sintering powder aggregates show that the dominant effect of TALH on the sintering mechanics is to increase the interparticle contact size, while the coordination number remains essentially unchanged.

These insights are used to develop generalized guidelines for designing reactive binders to mitigate creep, quantitatively highlighting the benefits of a high solid yield from binder decomposition.

Keywords: binder jet 3D printing, ceramics, sintering, powder processing, creep

1. Introduction

Binder jet 3D printing is an additive manufacturing process that builds net-shaped components, layer-by-layer, by selectively joining powder particles with a binder. The resulting green body is often friable, with a low relative density in the range of 0.4 to 0.7 [1, 2]. Thus, binder jet 3D printed parts must be strengthened using a post-processing densification method such as pressureless sintering. Retaining the shape of the as-printed component during densification processes can be difficult for several reasons. First, the low relative density of binder jet 3D printed green bodies means that achieving full density requires linear shrinkages of order 10% [1, 3, 4]. While the green body can be scaled to compensate for shrinkage, random variations in the extent of shrinkage can limit the dimensional accuracy of the final component to ~0.25% [5]. Other challenges include distortion resulting from gravitational body forces, friction between the part and the setting, and spatial variations in sintering rates [1, 2, 6]. While shrinkage and distortion are problems in conventional powder-processing, they are especially important in the context of binder jet 3D printing where the intent is to make complex shapes, and where the low particle coordination number and small interparticle contact area within binder jet 3D-printed parts leaves them particularly susceptible to distortion during early stages of sintering.

A promising approach to mitigating distortion in binder jet 3D printed materials is to treat the green body with additives that increase the relative density prior to sintering. These additives modify the structure of the preform, increasing the particle coordination number and the interparticle contact size. Several additives have been demonstrated experimentally, including metallic salts [7-10], metallo-organic inks [11], sol-gel inks [12], nanoparticle suspensions [13-15], and preceramic polymers [16-20]. Among these examples, reactive binders that are initially liquid and then decompose into solids on heating are attractive because they can be deposited without clogging the printhead [7, 11, 19, 21]. Such reactive binders have been shown to decrease shrinkage [13, 22] and mitigate creep during sintering of binder jet 3D printed components with unsupported features, e.g., cantilever beams. While reactive binders are routinely used, there are limited studies that link the effects of the reactive binder to the rates of densification and creep in sintering 3D printed agglomerates. Additionally, studies on sintering powder compacts indicate that altering the microstructure of the interparticle contacts (e.g., via reactive binder treatment) may slow the densification kinetics, an undesirable side effect [23, 24]. These observations suggest a potential tradeoff between mitigating distortion due to creep and achieving rapid densification for certain reactive binder systems.

The aim of this study is to gain insight into the effect of reactive binders on the mechanisms of creep and densification rates in binder jet 3D printed components. We consider a model reactive binder, aqueous titanium bis-ammonium lactato dihydroxide (TALH). TALH is a water-soluble titanium complex in which oxygen in hydroxyl and carboxyl groups, provided by lactic acid molecules, chelate to titanium forming a stable compound [25]. Thermolysis in the presence of oxygen decomposes the chelating ligands at temperatures

above 500 °C allowing for crystallization of TiO_2 [25, 26]. In previous work, we demonstrated that TALH addition can mitigate distortion in sintering binder jet 3D printed TiO_2 cantilever beams as shown in **Figure 1** [22]. In the present work, we extract creep and densification parameters (e.g., uniaxial viscosity, viscous Poisson's ratio, and sintering stress) by combining structural characterization and loading dilatometry experiments on sintering TALH-treated TiO_2. These parameters are then compared with analytic micromechanical models to reveal how the reactive binders modify the interparticle contact network and the resulting creep and densification behaviors. Finally, this analysis is used to develop quantitative guidelines for designing reactive binders to mitigate distortional creep.

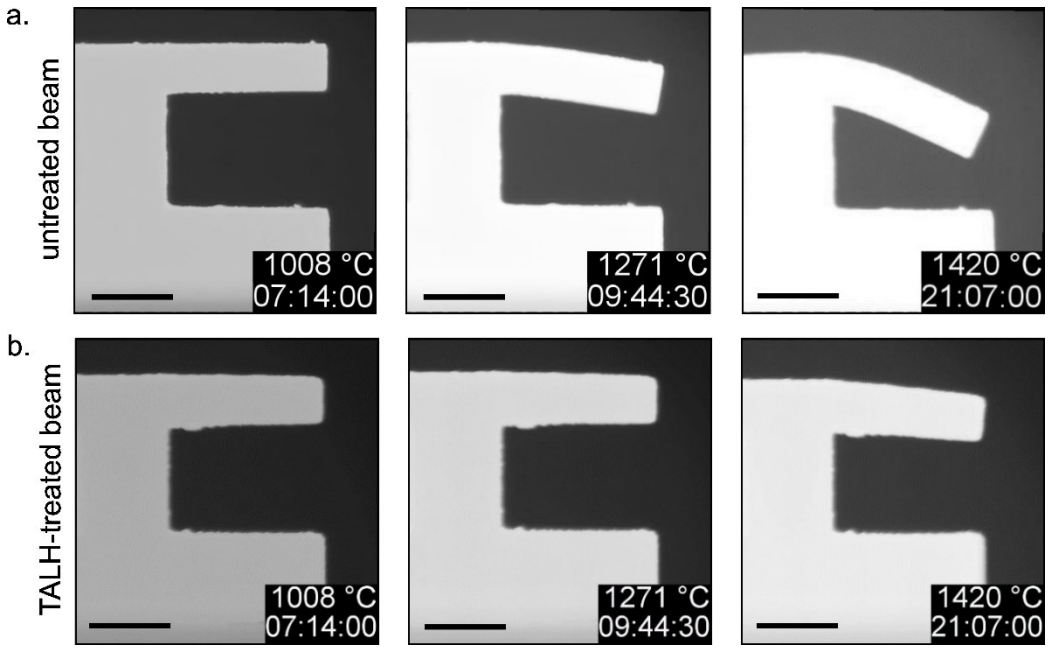

Figure 1: *In situ* images of sintering (a) untreated and (b) TALH-treated TiO_2 cantilever beams prepared via binder jet 3D printing.[22] Note that TALH treatment mitigates slumping of the unsupported beam. Instantaneous temperature and time are shown. Scale bars are 5 mm.

2. Experimental methods

The sintering behaviors of TALH-treated, binder jet 3D-printed TiO_2 were characterized using loading dilatometry experiments. Cylindrical test specimens with a diameter of 6.5

mm and a height of 6.5 mm were printed in an ExOne Innovent binder jet 3D printer using rutile TiO_2 powder (Saint-Gobain 1000) with an irregular particle shape and a mean particle size of 9 μm. The specimens were printed using an aqueous binder (ExOne, item number 7100037CL), with a saturation level of 90% and a layer thickness of 100 μm. After printing, the powder bed was heated to 180 °C for 4 hours to cure the binder. Prior to TALH treatment, the test specimens were strengthened by sintering in air at 1100 °C for 1 hour; This initial sintering step is referred to as pre-sintering. These pre-sintered samples were immersed in an aqueous TALH solution (50 wt% TALH, Sigma Aldrich) for 15 minutes, then heated in air at a rate of 3 K/min to 600 °C, to decompose the TALH into solid TiO_2.

Isothermal loading dilatometry experiments were performed using a NETSCH 402 F1 Hyperion thermomechanical analysis (TMA) system. The test temperature was varied over the range 1250 to 1450 °C, and the samples were heated at a rate of 12 K/min. The applied load was varied between 0.02 and 2 N, corresponding to an initial applied stress σ_z of 0.6 to 60 kPa. A low pre-load of 15 mN was applied during heating to maintain contact between the pushrod and the specimen while limiting the influence of the dilatometer prior to reaching the sintering temperature. At regular time intervals, the radial and axial lengths were measured using a micrometer and the sample density was calculated using mass and volume measurements. The relative density ρ of each sample was calculated by dividing the measured density by the theoretical density of rutile TiO_2 (4.23 g/cm^3). Recovered samples were characterized using an FEI Quanta 400 Scanning Electron Microscope (SEM).

3. Experimental results and discussion

3.1 Structural characterization

Figure 2a and **b** compare SEM micrographs of a pre-sintered TiO_2 specimen (without TALH) and a TALH-treated specimen heated to 600 °C. The average relative density of the compacts prior to pre-sintering was 0.38. Pre-sintering increased the relative density to 0.41 and formed submicron interparticle necks, examples of which are labeled in **Figure 2a**. During pre-sintering, the average axial and radial densification strains are 0.023 and 0.025, respectively. Hence the specimen shrinks only slightly, while forming interparticle necks with dimensions of 0.7 μm. These interparticle necks provide sufficient strength for TALH treatment. TALH treatment resulted in a TALH-derived submicron-thick layer of nanocrystalline TiO_2 that coated the particles and increased the interparticle contact size (**Figure 2b**). In our previous work, X-ray diffraction of TALH-derived TiO_2 heated to 500 °C revealed a mixture of anatase and rutile, while material heated above 700 °C was phase-pure rutile. The TALH-derived TiO_2 in **Figure 2b** is thus likely a mixture of anatase and rutile [22]. The TALH treatment increased the relative density to 0.43. When compared to our previous results, which showed that the TALH solution yields 17 wt% solid TiO_2, the TALH-derived increment in density reported here indicates that prior to binder decomposition, the pores were filled completely with TALH solution [22]. The thickness of the TALH-derived TiO_2 coating is estimated to be 0.6 μm (by assuming that the aggregate consists of spherical particles, with a homogeneous particle size of 9 μm, which are evenly coated by the TALH-derived TiO_2). After holding the TALH-treated material at 1350 °C for 135 minutes, typical sintering conditions, the TALH-derived coating was no longer visible (**Figure 2d**). This result is consistent with grain growth calculations, presented in

Appendix A, which show that the initially nanocrystalline TALH-derived TiO_2 overlayer is consumed by the microcrystalline particle core by ~1000 °C after heating from room temperature at 12 K/min. Comparing **Figures 2c** and **d** show that the untreated and TALH-treated specimens have qualitatively similar structures at sintering temperatures.

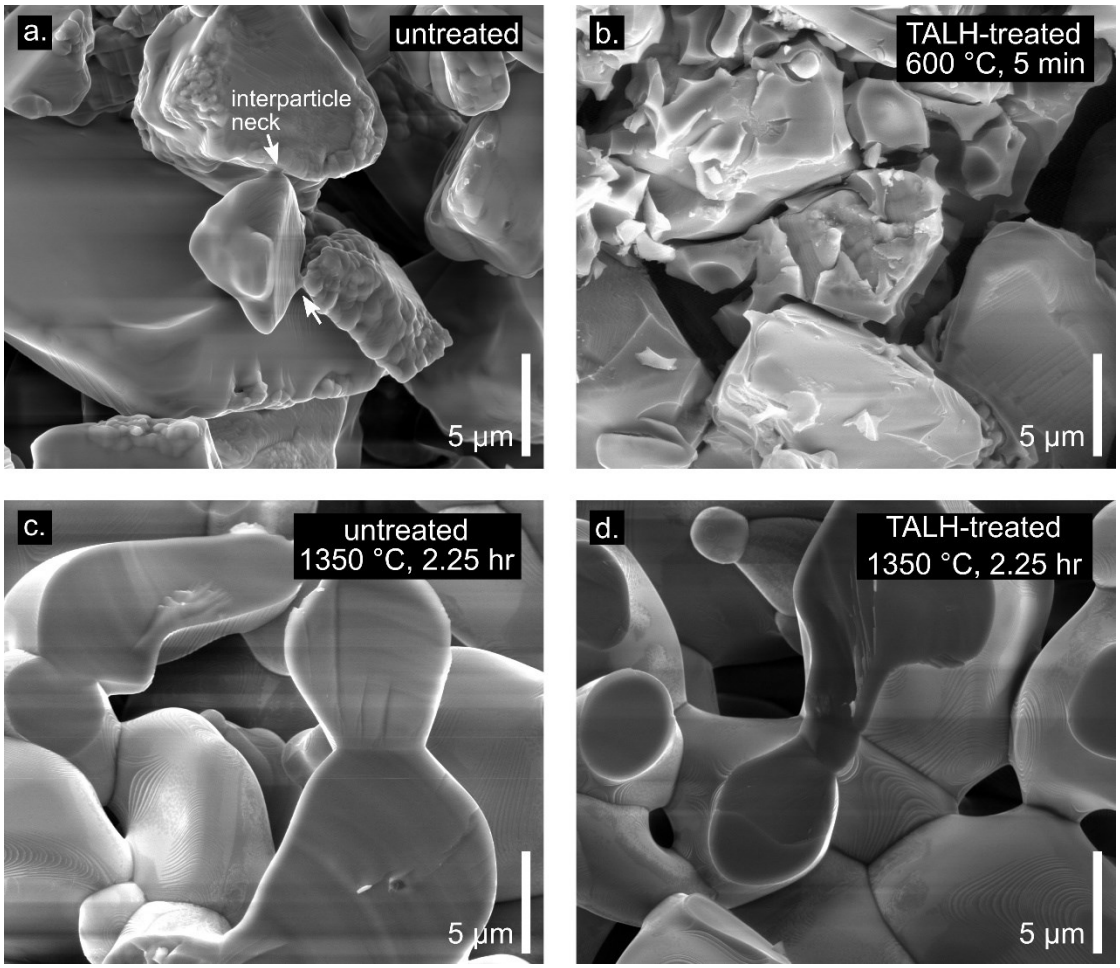

Figure 2: SEM micrographs of (a) an untreated TiO_2 sample that shows necks formed after pre-sintering by heating to 1100 °C for 1 hour and (b) a TALH-treated TiO_2 sample with TALH-derived TiO_2 coating the particles and increasing the interparticle contact area. (c) Untreated and (d) TALH-treated TiO_2 samples after holding at 1350 °C for 135 minutes under an axial stress of 30 kPa.

3.2 Creep and densification behaviors

Figure 3 shows the axial shrinkage ε_z as a function of time for specimens sintered under the normal stresses indicated. The axial shrinkage increases with applied stress in both the untreated and the TALH-treated specimens, but the magnitude of the axial shrinkage is

always lower in the TALH-treated material. The axial shrinkage contains contributions from both densification and creep. To deconvolute these effects, periodic measurements of the radial strain ε_r and axial strain ε_z were used to compute the densification strain ε_ρ and creep strain ε_c as follows [27]

$$\varepsilon_\rho = \frac{1}{3}(\varepsilon_z + 2\varepsilon_r), \quad (1)$$

$$\varepsilon_c = \frac{2}{3}(\varepsilon_z - \varepsilon_r). \quad (2)$$

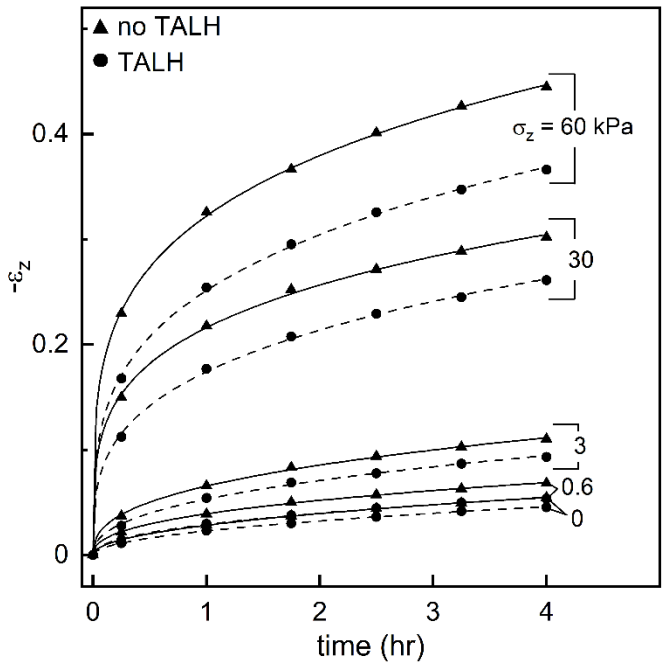

Figure 3: Axial shrinkage strain -ε_z of specimens sintered at 1350 °C under varying uniaxial stresses σ_z plotted as a function of sintering time. While all samples exhibit stress-dependent strain, the untreated (no TALH) material shows greater stress sensitivity than the material treated with TALH.

Figure 4 shows the densification ε_ρ and creep ε_c strains under different applied stresses. The magnitudes of ε_ρ in **Figure 4a** clearly demonstrate that the applied stress accelerates densification. The untreated material consistently had a larger ε_ρ than the TALH-treated material, even under no applied stress. This result is in line with observed reductions in shrinkage for binder jet 3D printed 410 SS treated with Fe nanoparticles [13] and in Al_2O_3

preforms treated with metal salts [9]. The creep strain also increased with applied stress (**Figure 4b**). For untreated and TALH-treated material, the creep strain is roughly three times greater than the densification strain, highlighting the importance of creep in sintering powder aggregates, even under low applied stresses.

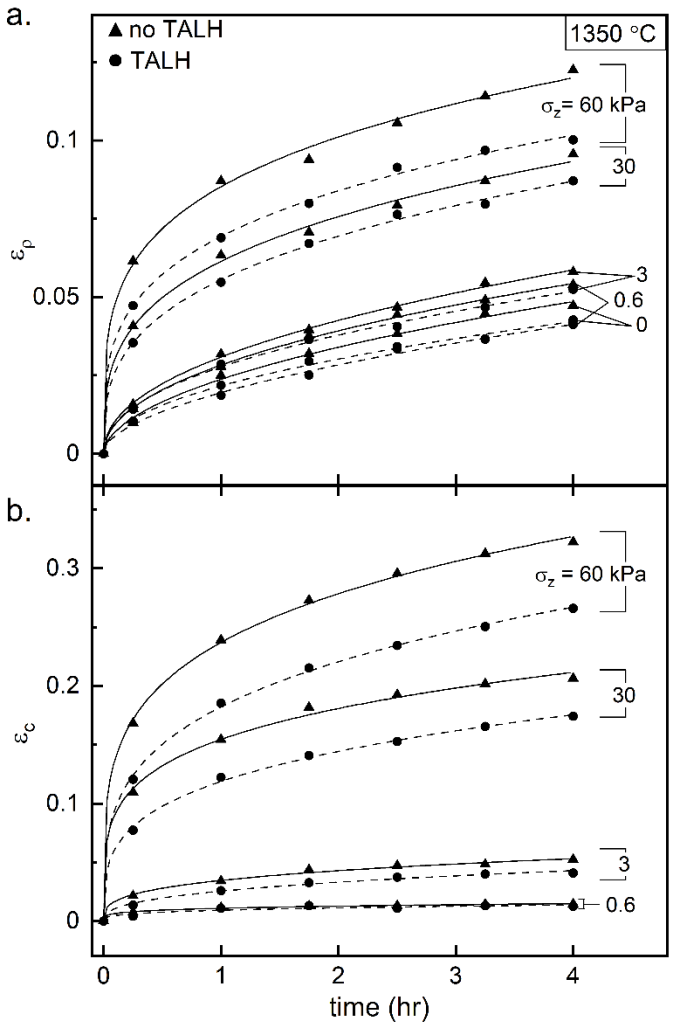

Figure 4: Measured strain (a) densification strain ε_ρ and (b) creep strain ε_c of TALH-treated and untreated specimens sintered at 1350 °C under varying uniaxial stress σ_z, plotted as a function of sintering time.

Figure 5 and **6** show, respectively, densification and creep rates calculated using the data in **Figure 4**. Densification and creep are fastest during the first hour of sintering when small interparticle contacts provide a high driving force for sintering and minimal resistance to shear deformation. Interestingly, the untreated specimens densify faster than

the TALH-treated material at fixed time under the full range of applied stresses (**Figure 5a)**; however, plotting the densification rate against instantaneous relative density, as in **Figure 5b**, shows that under most conditions, the TALH-treated materials densify faster than their untreated counterparts at equivalent relative density. Similar behavior is seen in the creep rate data in **Figure 6**: at fixed time, the untreated material creeps faster than the TALH-treated material, while at equivalent relative density, the behavior is reversed, and the TALH-treated specimens creep more rapidly. These results, considered together, demonstrate that, despite the similar appearance of the untreated and TALH-treated specimens in **Figure 2**, there are sustained differences in their respective structures which give rise to distinct densification and creep behaviors.

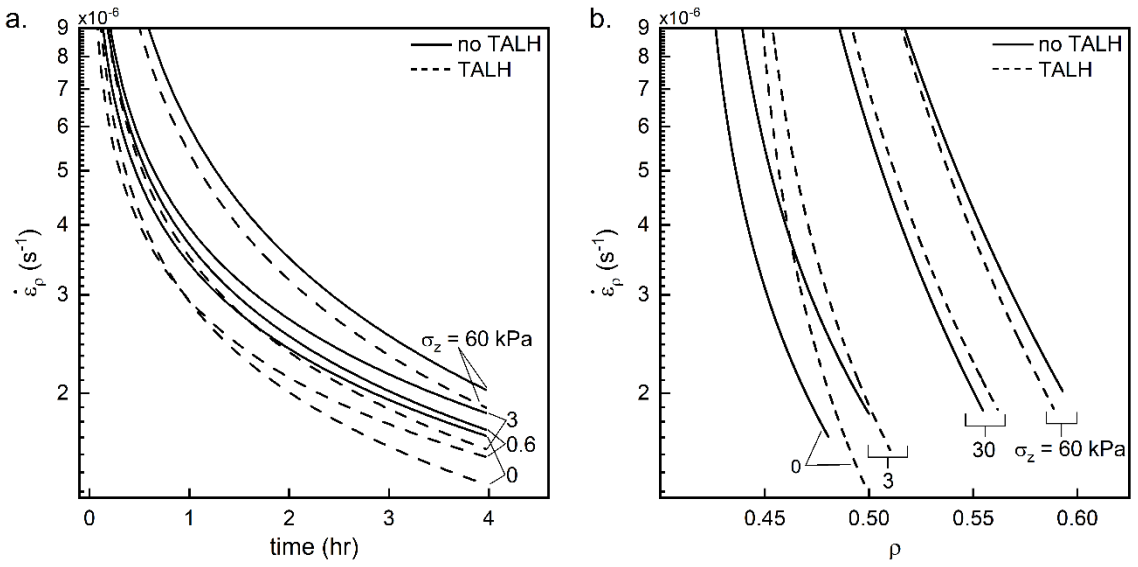

Figure 5*:* Uniaxial densification rate $\dot{\varepsilon}_\rho$ as a function of (a) time and (b) relative density ρ for TALH-treated (TALH) and untreated (no TALH) specimens under the indicated uniaxial stress σ_z. All specimens were sintered at 1350 °C.

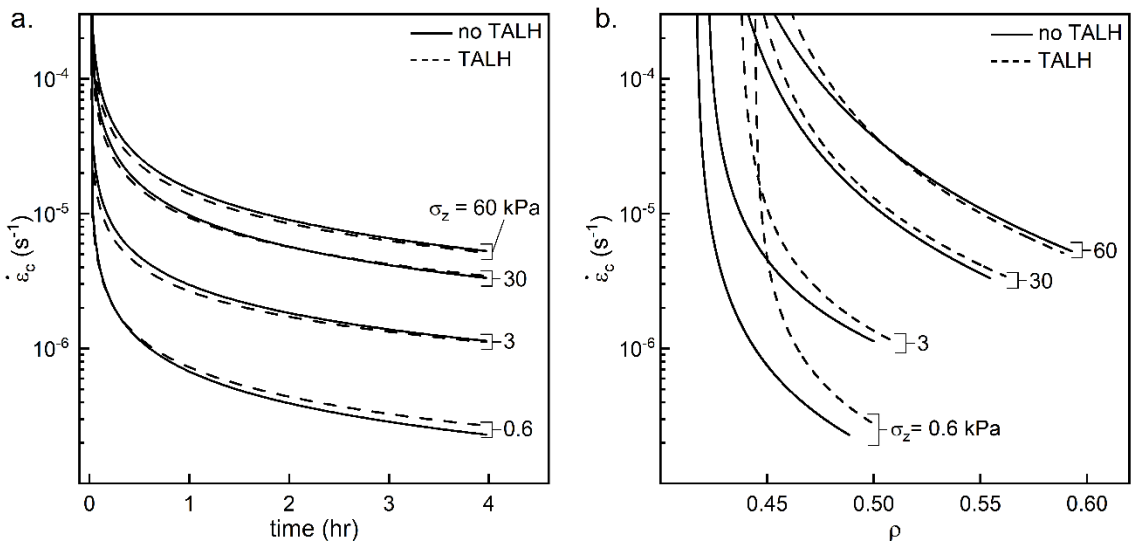

Figure 6: Creep strain rate $\dot{\varepsilon}_c$ as a function of (a) time and (b) relative density ρ for the untreated (no TALH) and TALH-treated (TALH) specimens under varying uniaxial stress σ_z. All specimens were sintered at 1350 °C.

3.3 Creep mechanisms in TALH-treated material

A potential explanation for the distinct creep behaviors of neat and TALH-treated TiO_2 is that TALH treatment modifies the creep mechanism. To test for such effects, the stress exponent n and creep activation energy Q in the generalized creep expression

$$\dot{\varepsilon}_c = A\sigma^n \exp\left(\frac{-Q}{RT}\right) \quad (3)$$

were measured for both materials. **Figure 7a** shows the creep rate $\dot{\varepsilon}_c$ for the untreated and TALH-treated materials as a function of applied stress at fixed ρ = 0.49. Both datasets are well-described by linear fits which give stress exponents of order unity. **Figure 7b** summarizes the measurements of the stress exponent for the untreated and TALH-treated materials over the full range of relative density. The untreated specimens have a higher stress exponent than the TALH-treated material, but in both cases, the stress exponent decreases with increasing relative density, approaching unity. The stress exponent exhibited by both materials at low relative densities indicate that power-law creep (with n ≥ 3) may contribute to the creep rate at early stages of sintering.

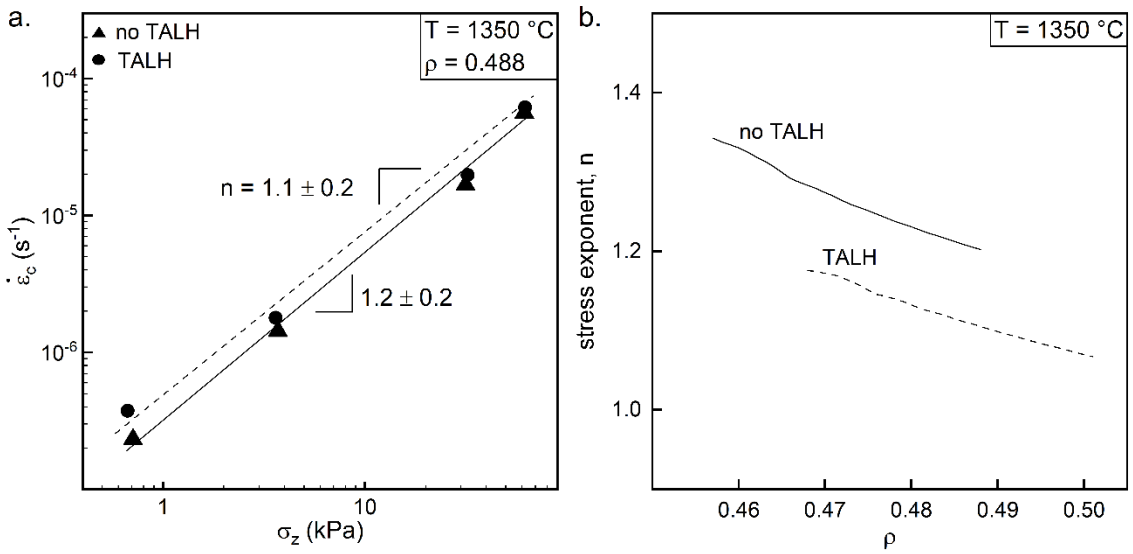

Figure 7: Stress exponent analysis showing (a) creep strain rate $\dot{\varepsilon}_c$ as a function of applied stress σ_z, with a linear fit for calculating the stress exponent n for both TALH-treated and untreated specimens at a relative density of 0.49 and (b) stress exponent n as a function of relative density ρ for both TALH-treated and untreated specimens. The uncertainty is determined using 90% confidence bounds for the fitted data.

The activation energy for creep Q was determined by sintering at temperatures of 1250, 1350, and 1450 °C, under an applied stress of 30 kPa. **Figure 8** is an Arrhenius plot which shows $\dot{\varepsilon}_c$ at a fixed relative density of 0.51, the overlaid linear fits give an activation energy of roughly 400 kJ/mol for both the TALH and the untreated materials. While the observed activation energy of ~400 kJ/mol is higher than that reported for grain boundary diffusion in nominally pure rutile TiO_2 (320 kJ/mol) [28], it is consistent with the theoretical activation energy of 400 kJ/mol observed for lattice diffusion in rutile TiO_2 with intrinsic point defects [29-31] (cf. **Appendix B**). Importantly, the above analysis indicates that there are no significant differences in the dominant creep mechanism for TALH-treated and untreated material.

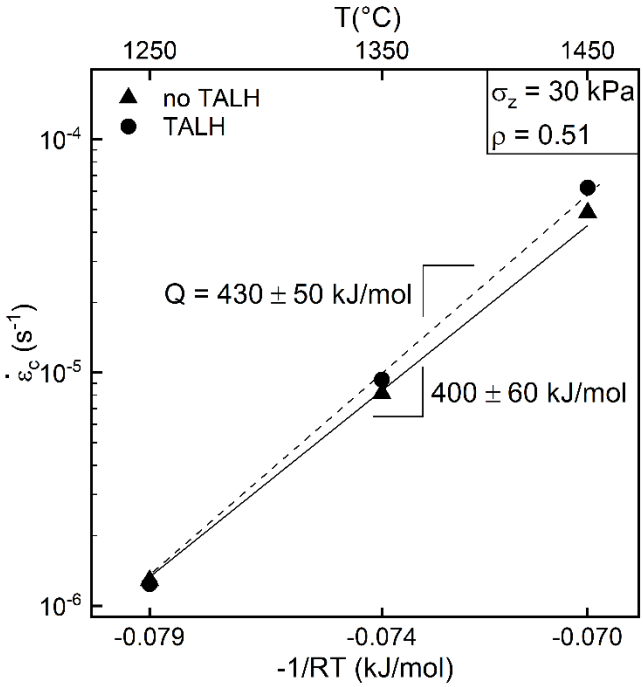

Figure 8: Activation energy analysis showing creep strain rate $\dot{\varepsilon}_c$ as a function of temperature with linear fit for calculating the activation energy Q for both TALH-treated and untreated specimens at a relative density ρ of 0.51. The uncertainty is determined using 90% confidence bounds for the fitted data.

The stress exponents and activation energies in **Figure 7** and **8** indicate that diffusion-mediated creep dominates in both neat and TALH-treated TiO_2. However, the monotonically decreasing stress exponent in **Figure 7b** suggests that power law creep may contribute during the early stages of sintering. This result is interpreted by comparing the contact stresses and sintering temperatures in the present experiments with the deformation mechanism map shown in **Figure 9**, calculated using material data for rutile TiO_2 available in [30]. Following Helle et al. [32], the mean contact stress, σ_c, between particles can be approximated as

$$\sigma_c = \frac{\sigma_z(1-\rho_0)}{\rho^2(\rho-\rho_0)}, \qquad (4)$$

where ρ_0 is the initial relative density prior to TALH treatment and sintering. Here, ρ_0 is set to 0.41, corresponding to the average relative density after pre-sintering, and further

increments in relative density are due to TALH treatment (for treated specimens) and sintering. For comparison with the deformation mechanism map in **Figure 9**, the contact stress is normalized by the temperature-dependent shear modulus μ of TiO_2, and the deviatoric component is calculated by dividing this normalized contact stress by $\sqrt{3}$. The material constants used to construct the deformation mechanism map are summarized in **Appendix C**. The datapoints in **Figure 9** represent experimental values of the normalized shear stress $\sigma_c/\sqrt{3}\mu$, calculated using **Equation 4**, as a function of homologous temperature T/T_m at various dwell times.

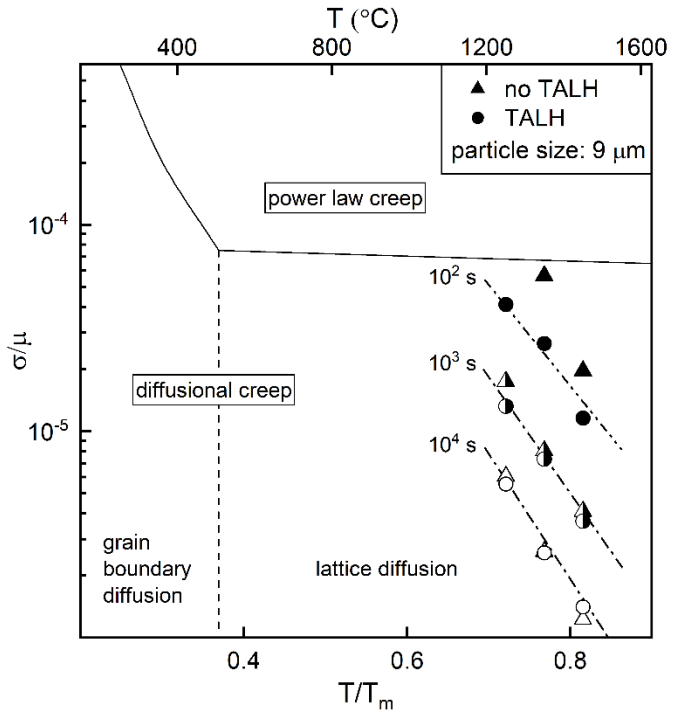

Figure 9: Deformation mechanism map showing regions of normalized stress and temperature where a single mechanism dominates. This map was constructed using material data from Ref. 30. Data points show experimental measurements obtained in the present study with symbols and trend lines indicating the total time at sintering temperature.

In **Figure 9,** the experimental datapoints measured at the early stages of sintering ($t=10^2$ sec.) are near the power law creep boundary, indicating a contribution of power law creep. After two hours of sintering, the data lie squarely in the diffusional creep regime, consistent

with the stress exponent gradually approaching unity with increasing relative density. When comparing the untreated and TALH-treated materials, initially, the increase in relative density afforded by TALH decreases the magnitude of the contact stress; however, this difference is diminished when sintering for longer than 10^2 seconds, as the microstructure in both cases evolves to be similar.

Critically, the measurements of the stress exponent and activation energy reveal that TALH treatment does not change the creep mechanism, with both the untreated and TALH-treated materials deforming via lattice-mediated diffusional creep. The predicted grain size of the TALH-derived material (~10 μm) also supports lattice-mediated diffusional creep. Most importantly, TALH treatment decreases the contact stresses during the early stages of sintering when the component is most susceptible to distortion. This effect of TALH treatment emphasizes the importance of the interparticle connectivity for mitigating creep. While the creep mechanism is unchanged, the observed differences in the creep and densification rates between TALH and untreated material compared at the same relative density (**Figure *5*b** and **Figure *6*b**) indicate that microstructural differences persist.

4. Structure-sensitive constitutive models of sintering mechanics

The diffusional creep behaviors of the neat and the TALH-treated materials motivate a linear viscous constitutive law, commonly used in descriptions of sintering solids [4, 33, 34], of the form

$$\dot{\varepsilon}_z = \dot{\varepsilon}_f + \frac{1}{E_p}[\sigma_z - N(\sigma_r + \sigma_\theta)], \tag{5}$$

where $\dot{\varepsilon}_z$ is the axial strain rate, E_p is the uniaxial viscosity, N is the viscous Poisson's coefficient, and $\dot{\varepsilon}_f$ is the free strain rate, i.e., the densification strain rate in the absence of

applied stresses. The axial, radial, and circumferential stresses are represented by σ_z, σ_r, and σ_θ, respectively. Importantly, there are physical models that directly relate $\dot{\varepsilon}_f$, E_p, and N to the structure of the sintering powder aggregate [35]. Thus, differences in these parameters for the neat and TALH-treated materials can provide insight into how the TALH-derived TiO_2 overlayer modifies the microstructure and resulting sintering mechanics.

The uniaxial viscosity term represents the ability for the sintering compact to resist deformation under an external load. Under uniaxial compression, **Equation 5** can be solved for the uniaxial viscosity E_p:

$$E_p = \frac{\sigma_z}{\dot{\varepsilon}_z - \dot{\varepsilon}_f}. \quad (6)$$

Calculations of E_p using this expression with the experimental data are summarized in **Figure 10**. The uniaxial viscosity increases with relative density, with magnitudes between 0.01 and 10 GPa·s. This range is in line with the uniaxial viscosities of 0.1 to 6 GPa·s observed during initial stage sintering of ceramic compacts of YSZ, NiO-YSZ [36] and $BaTiO_3$ [37] with similarly low relative densities, ρ = 0.45–0.55. The data for the TALH-treated material is offset to higher relative density at the start of sintering due to the mass increase from the TALH addition. Notably, the TALH-treated TiO_2 has a lower uniaxial viscosity than that of the untreated material when compared at the same relative density under an applied stress of 0.6 kPa. This result aligns with the similar observation of the lower creep rates of the untreated material in **Figure 6b**. While the TALH-treated material has a lower uniaxial viscosity at equivalent relative density, the TALH addition prior to sintering minimizes the overall creep at the initial stage of sintering when creep is fastest.

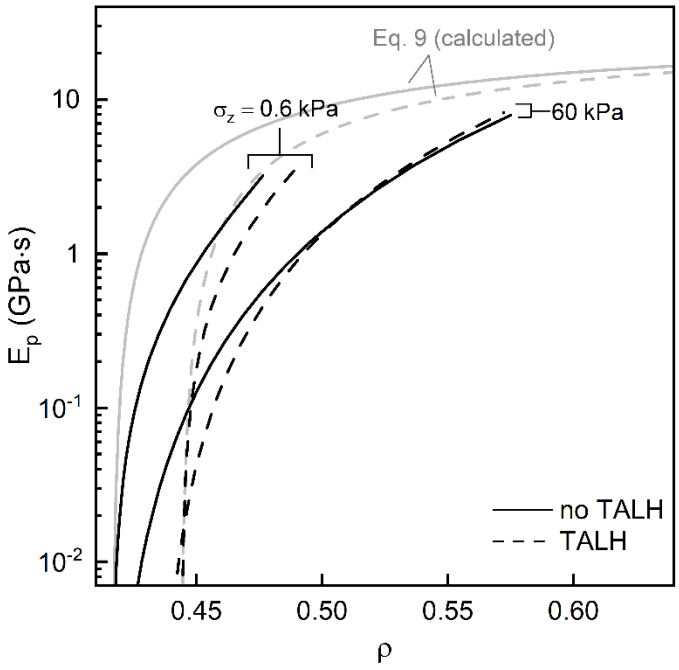

Figure 10: Uniaxial viscosity E_p as a function of relative density ρ for untreated and TALH-treated specimens sintered at 1350 °C.

The viscous Poisson's ratio N is shown in **Figure 11**. For the untreated material, N begins as low as 0.1 and increases to 0.5 as the compacts densify. For the TALH-treated material, the range of N is smaller, between 0.1 and 0.35. At the same relative density, the untreated material exhibits a higher N than the TALH-treated material; for both cases, the N values are load-dependent, reflecting differences in microstructure induced by the applied stress. The magnitude of N = 0.2–0.5 is consistent with previously reported theoretical and experimental values for sintering powder compacts. However, the rate of increase in previous reports is slower, linearly increasing over a range of ρ = 0.4 to 1 [38-40], whereas in the present study, the range of ρ is 0.43 to 0.46. This discrepancy in the rate of increase of N may result from microstructural anisotropy induced by the axial loading.

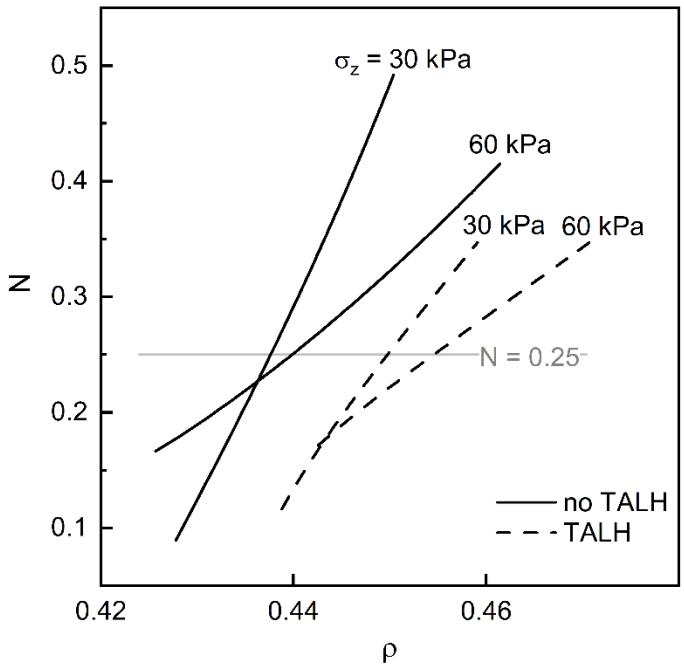

Figure 11: Viscous Poisson's ratio *N* plotted as a function of relative density ρ for TALH-treated and untreated materials sintered at 1350 °C

The uniaxial sintering stress, σ_s, is the tensile stress that prevents densification along the loading direction. It is a result of the thermodynamic driving force for densification and is a function of surface energy and curvature of the pore network [35]. The uniaxial sintering stress is determined by setting $\dot{\varepsilon}_z = 0$ in **Equation 6,** then solving for σ_z:

$$\sigma_s = -\dot{\varepsilon}_f E_p. \tag{7}$$

Calculations of σ_s using this expression with the experimental data are shown in **Figure 12**. The uniaxial sintering stresses for the TALH-treated and neat materials begin around 2 kPa and increase with relative density to 15–20 kPa when $\rho = 0.60$. When compared at the same relative density, the TALH-treated material has a slightly lower uniaxial sintering

stress than the untreated material, indicating a lower thermodynamic driving force for sintering.

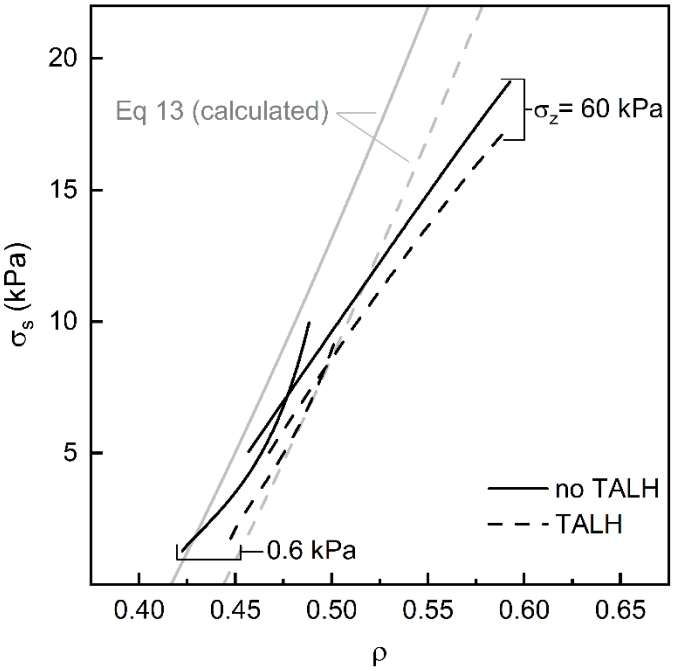

Figure 12: Uniaxial sintering stress σ_s as a function of ρ for untreated and TALH-treated specimens sintered at 1350 °C

When densification is accompanied by pore coarsening, the sintering stress has been shown to decrease with increasing relative density [4, 41]. However, in the absence of pore coarsening, shrinkage increases the curvature of the pores which results in a sintering stress that increases with relative density [42, 43]. The increase in sintering stress shown in **Figure 12** indicates that there is minimal coarsening of the pore network in both the TALH-treated and untreated materials during sintering. The lower sintering stress in the TALH-treated material than in the untreated material can be explained using the approximation [44, 45]

$$\sigma_S \approx \frac{2\gamma_S}{r_0}, \tag{8}$$

where r_0 is the mean radius of curvature of the pore surface and γ_s is the average surface energy, which, for rutile TiO_2, is ~0.6 J/m^2 [28]. During the initial and intermediate stages of sintering, new contacts are forming which lowers r_0 and increases the sintering stress. At later stages of sintering, when no new particle contacts are formed, capillary forces are reduced, resulting in an observed decrease in the sintering stress above ρ = 0.95 [42]. The mean radius of curvature r_0 can be estimated by combining the experimentally measured sintering stress with **Equation 8**, resulting in values on the order of 100 μm for both the untreated and TALH-treated materials. When σ_z = 0.6 kPa, the mean radius of curvature in the TALH-treated material is roughly 30% larger than that in the untreated material. This difference is likely because the TALH-derived TiO_2 increases the local radius of curvature at the interparticle necks, thus decreasing the driving force for sintering.

Previous sintering studies on CdO and Al_2O_3 compacts showed that stress-assisted densification was significant when the applied stress was greater than the sintering stress [4, 41]. Similar behavior is also observed in the present study: the applied stress dramatically accelerates densification when $\sigma_z > \sigma_s$, as seen in **Figure 4**. Further, comparing the densification rates of the TALH-treated and neat materials in **Figure 5b** shows that the materials have dissimilar densification rates when $\sigma_z < \sigma_s$ (σ_z = 0.6, 3 kPa), reflecting sustained differences in their respective microstructures. However, the densification rates converge when the applied stress exceeds the sintering stress (σ_z = 30, 60 kPa) and extrinsic stress-assisted densification starts to dominate regardless of structure.

The TALH treatment decreases the uniaxial viscosity, effective Poisson's ratio, and sintering stress when compared with untreated material at the same relative density. The

lower uniaxial viscosity indicates that the TALH-treated material has a lower load-bearing area than the untreated material, while the lower sintering stress indicates that the mean radius of curvature of interparticle necks in the TALH-treated material is larger than that in the untreated material. These effects highlight the important role of particle coordination number, size of the interparticle necks, and radius of curvature at the necks. The lower range of effective Poisson's ratio for the TALH-treated material is closer to the predicted effective Poisson's ratio exhibited by compacts sintering without an externally applied load [39]. Additionally, when the applied stress is less than the sintering stress, the applied stress has a weak effect on the densification rate of the TALH-treated material.

5. Modeling the effects of TALH treatment on sintering mechanics

The microstructural characterization and loading dilatometry experiments show that TALH treatment decreases the average contact stresses at early stages of sintering and point to the importance of the interparticle contact area for mitigating creep. We now estimate how TALH treatment modifies the fractional contact area A_f, defined as the total contact area per particle normalized by the particle surface area, and the resulting sintering mechanics using models developed by Arzt [42] then later expanded by McMeeking and Kuhn [35].

Models developed by McMeeking and Kuhn using virtual power arguments link microstructural parameters (e.g., particle coordination number, interparticle contact area, and particle size) to macroscopic creep parameters (e.g., bulk viscosity, shear viscosity) in a sintering compact [35]. Using the results for the bulk and shear viscosities from McMeeking and Kuhn, the uniaxial viscosity is

$$E_p = \left(\frac{\rho_0}{\rho}\right)^{\frac{2}{3}} \frac{A_f^2 R_0^3}{24\mathfrak{D}}, \tag{9}$$

where R_0 is the initial particle radius and $\mathfrak{D}$ is an effective diffusivity given by

$$\mathfrak{D} = \frac{(\delta D_b + r_n D_v)\Omega}{kT}. \quad (10)$$

Because the sintering temperatures of 1250-1450 °C are sufficiently high that the TALH-derived TiO_2 is rutile [22], material properties for rutile TiO_2 are used to calculate the effective diffusivity. These same material properties were used to construct the deformation mechanism map (cf. **Appendix C**). In **Equation 10**, δD_b is the product of the grain boundary diffusion coefficient and the boundary thickness, D_v is the lattice diffusion coefficient, Ω is the atomic volume, k is Boltzmann's constant, T is the absolute temperature, and r_n is the radius of curvature at the neck. When densifying mass-transport mechanisms dominate, the radius of curvature at the neck can be estimated using [46]

$$r_n \approx \frac{{x_d}^2}{4(R_0 - x_d)}. \quad (11)$$

When non-densifying mass-transport mechanisms dominate, the radius of curvature is approximately [46]

$$r_n \approx \frac{{x_n}^2}{2(R_0 - x_n)}, \quad (12)$$

where x_d, and x_n are the radii of the neck formed through densifying mechanisms and non-densifying mechanisms, respectively.

The expressions for bulk and shear viscosities developed by McMeeking and Kuhn can also be used to estimate the viscous Poisson's ratio N. The result is a constant, N = 0.25, independent of relative density, as shown in **Figure 11**. Setting N to 0.25 for the present range of relative density, ρ = 0.4–0.6, is a suitable approximation when compared to constitutive models for N that increase from 0 to 0.25 in this range [39].

Lastly, McMeeking and Kuhn developed the following expression for sintering stress in the case of rapid surface diffusion:

$$\sigma_s = A_f \rho \left(\frac{\rho_0}{\rho}\right)^{\frac{1}{3}} \left(\frac{2\gamma_s}{R_0}\right)(1 - 2N). \tag{13}$$

This expression was used to compute the sintering stress curves in **Figure 12**, where the sintering stress is observed to increase with relative density. Additionally, the TALH-treated material has a lower sintering stress than the untreated material at equivalent relative density. Fair agreement in both cases suggests that the models proposed by McMeeking and Kuhn are valid for quantifying differences in material properties between the untreated and TALH-treated materials.

Equations 9 and **13** reveal that differences in initial relative density and fractional contact area A_f for TALH-treated and untreated materials will contribute to differences in uniaxial viscosity and sintering stress. Here, we quantify the effect of the TALH treatment on A_f, expressed as

$$A_f = \frac{Za}{4\pi R_0^2}, \tag{14}$$

where the product of the mean coordination number Z and the mean interparticle contact area a is normalized by the total particle surface area. Following Arzt [42], the increase in coordination number of a compact densifying through either TALH treatment or sintering can be approximated using the radial distribution function for a powder aggregate:

$$Z = Z_0 + C\left[\left(\frac{\rho}{\rho_0}\right)^{\frac{1}{3}} - 1\right], \tag{15}$$

where Z_0 is the initial coordination number, and C is the rate of increase in coordination number as a function of relative density. When TALH solution fully infiltrates the pores, the final relative density resulting from subsequent TALH decomposition is

$$\rho = \rho_0 + \phi(1 - \rho_0), \quad (16)$$

where ϕ is the volume fraction yield of solid material.

Arzt calculated Z and C using a cumulative radial distribution function for random close packed spheres for which $\rho_0 = 0.64$ [47, 48]. To account for the low initial relative density of $\rho_0 = 0.41$ in the present TiO_2 aggregates, Z_0 and C are calculated using the radial distribution functions predicted by discrete element method simulations from Yang et al. for loosely packed powder compacts (**Figure 7** in [45]). Combining the experimental values of $\rho_0 = 0.41$ with the radial distribution function proposed by Yang et al. results in $Z_0 = 3.6$ and $C = 10$. Using these terms with **Equation 15** gives the coordination number as a function of relative density plotted in **Figure 13**. At $\rho = 0.41$ for the untreated and $\rho = 0.43$ for the TALH-treated samples, **Equation 15** predicts coordination numbers close to 4. Thus, due to the loose packing in the as-printed material and the low solid yield from the TALH, the TALH treatment has a minor effect on the coordination number.

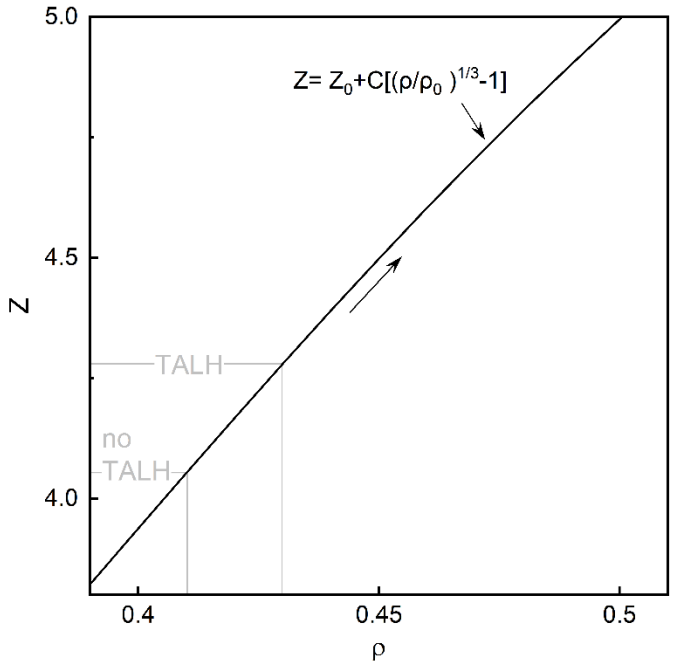

Figure 13: Coordination number *Z* as a function of relative density *ρ*.

Continuing with the framework proposed by Arzt, we evaluate the increase of the interparticle contact area within a densifying powder aggregate. This method models densification by increasing the size of particles within a fixed volume and, as the particle size is increased, redistributing material from regions where particles overlap. In compaction, material is redistributed as a uniform layer over the available particle surface [42]. During the TALH treatment, we observe that the TALH-derived TiO_2 is deposited uniformly over the surface of the contacts, but not at locations where particles would overlap. Considering this similarity in material redistribution, we use the following compaction model (**Equation 9** in Ref. 39) to compute the normalized area, *a*, of a single contact due to the TALH treatment:

$$\frac{a}{4\pi R_0^2} = \frac{1}{12ZR'^2}\left[3\left(R''^2 - 1\right)Z_0 + R''^2\left(2R'' - 3\right)C + C\right], \qquad (17)$$

where *R'* is the new particle radius due to the TALH addition and *R"* is the radius after TALH has been redistributed over the free surface area.

The material redistribution model for sintering differs from the model for TALH treatment. When the agglomerate densifies through sintering, excess material is deposited locally at the particle contacts. This results in the following equation developed by Arzt:

$$\frac{a}{4\pi R_0^2} = \frac{11}{4\pi R_0^2 Z R'}\left[Z_0(R'-1) + \frac{C}{2}(R'-1)^2\right]. \quad (18)$$

Using **Equations 17** and **18**, **Figure 14** plots the evolution of the interparticle neck area for the complete post processing cycle (pre-sintering, TALH treatment, and sintering). The trajectory through *ABC* captures the evolution of the normalized area of a single contact during sintering of the untreated samples, calculated using **Equation 18**. The TALH-treated samples follow a different trajectory – *ABB'C'*, where the evolution from *AB* and *B'C'* is due to sintering (calculated using **Equation 18**) while the evolution from *BB'* is due to the TALH treatment (calculated using **Equation 17**). For further comparison, the broken curve shows the evolution of a neck in an aggregate densified through pre-sintering and TALH treatment only (no additional sintering). Densifying via sintering results in a larger contact area than increasing to the same relative density through TALH treatment. However, prior to sintering, the TALH treatment increases the normalized contact area without requiring high temperatures that induce creep.

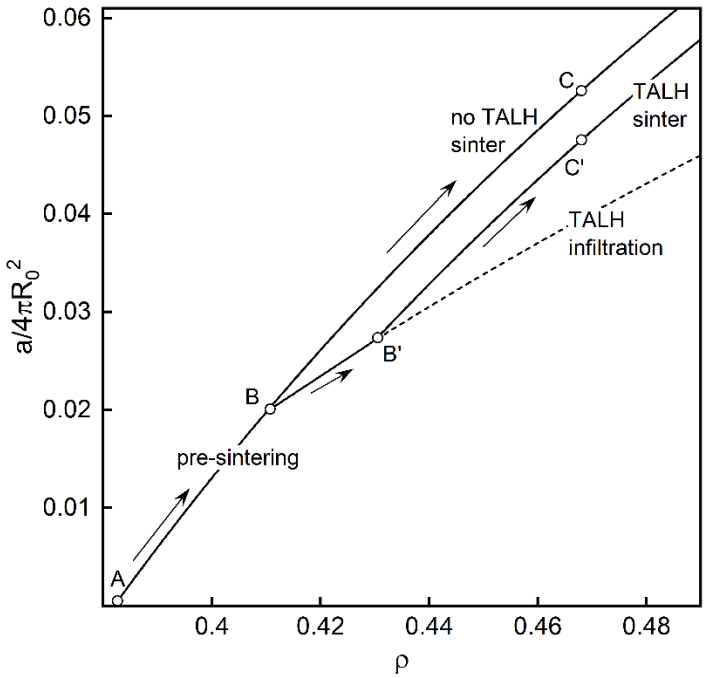

Figure 14: Fractional area of a single contact as a function of relative density ρ. Both untreated and TALH-treated samples begin at point A and evolve to point B during pre-sintering. Once pre-sintering is complete, the untreated sample is further sintered to point C. TALH treatment results in the observed increment from point B to point B'. After TALH treatment, the rate of increase is the same as that for sintering from B' to C'. The broken curve represents the neck size that can be achieved through TALH treatment alone following pre-sintering.

For the present study, sintering is treated as a densifying mechanism, where the neck radius x_d from **Equation 11** is calculated from the contact area in **Equation 18**. In contrast, TALH treatment is treated as a non-densifying mechanism, because it adds material to the neck without contributing to particle centroid approach, and x_n from **Equation 12** is calculated using the expression in **Equation 17**. The different contact areas from **Equations 11** and **12** result in similar values for radius of curvature in the TALH and untreated samples when compared at the same relative densities: r_n increases from ~1 nm to 1 μm as ρ increases from 0.41 to 0.64.

There are minimal differences in the evolution of the coordination number and the radius of curvature at the neck when sintering and infiltrating with TALH to the same relative density. However, as clearly shown in **Figure 14**, there is variation among the contact

areas, where differences in material redistribution result in a larger contact area due to sintering than TALH treatment. This larger contact area directly affects the uniaxial viscosity, viscous Poisson's ratio, and uniaxial sintering stress. In the calculations, the effect of the TALH treatment was addressed by updating the initial relative density ρ_0 from 0.42 to 0.44, corresponding to the relative density achieved by TALH addition. The equations for the evolution during sintering of the contact area and the radius of curvature (**Equations 18** and **11**) were then used to model the evolution of E_p, N, and σ_s. The results are overlaid in **Figure 10**, **11** and **12**, respectively, where there is excellent agreement between the calculations and the experimental results. This good agreement is somewhat surprising given the simplifying assumptions in the different models, e.g., monodisperse spherical particles.

The micromechanical model developed by McMeeking and Kuhn captures the physics of creep and densification in the TALH-treated and untreated materials. However, the model represents an ideal case where the applied stress does not result in an anisotropic microstructure. For this reason, the experimentally measured uniaxial viscosity of the TALH-treated material, which is less sensitive to the applied stress than the untreated material, is in excellent agreement with the calculated E_p when sintered under a low applied stress of 0.6 kPa. However, when the stress is increased to 60 kPa, both the TALH-treated and untreated material deviate from the model, indicating that the applied stress results in microstructural anisotropy. This anisotropy likely contributes to the deviation between the experimentally measured N and the N = 0.25 predicted by McMeeking and Kuhn [35]. As observed in the experiments, the calculated values for E_p and σ_s are lower in the TALH-treated samples when compared to the untreated samples sintered to the same

relative density. **Equations 17** and **18** reveal that variations in material properties result from differences in material distribution, where sintering results in larger interparticle necks than TALH treatment. The increase in fractional contact area A_f afforded by the TALH treatment produces compacts that are more sensitive to stress at the later stages of sintering than compacts brought to the same relative density through sintering alone. However, the TALH-derived material increases A_f prior to sintering, which increases the uniaxial viscosity and lowers the average contact stresses in the component at the early stages of sintering, resulting in less creep overall.

6. Implications for implementing reactive binders

The insights gained from studying the effects of TALH treatment on the microstructure of the aggregate and sintering mechanics are generalizable to other reactive binder and powder systems. When only considering the geometric differences of the microstructure, a higher A_f afforded by reactive binder treatment will lower the contact stresses within the component at early stages of sintering and increase the uniaxial viscosity. Accordingly, we have developed maps to assess the effect of different reactive binders on key variables contributing to the creep and densification behaviors, namely the number of contacts Z, the average normalized area of each individual contact $\bar{a}$, and the total fractional contact area A_f. We use these maps to compare three classes of reactive binders that have been described in the open literature: (i) soluble metal compounds [10, 11, 22]; (ii) nanoparticle (np) suspensions [13-15]; (iii) preceramic polymers [17, 18]. The following plots were generated using data for these different reactive binder systems, summarized in **Table 1**.

Table 1: Data on various combinations of powder and reactive binder reported in the open literature.

	base powder	particle size (μm)	ρ_0	reactive binder	precipitate	ϕ
soluble metal compound	Mo [10]	66	0.56	$Cu(NO_3)_2$	Cu	0.003
	Mo [10]	66	0.56	Ag_2CO_3	Ag	0.005
	Mo [10]	31	0.5	$[AgNO_3][Cu(NO_3)_2]$	Ag-Cu	0.021
	TiO_2 [22]	10	0.4	TALH	TiO_2	0.047
	Cu [11]	17	0.44	metal-organic ink	Cu	0.011
nanoparticle suspension	Cu [14]	17	0.44	np-Cu	Cu	0.022
	410 SS [13]	75	0.57	np-Fe	Fe	0.005
	CaO [15]	74	0.57	np-ZrO_2	ZrO_2	0.017
	CaO [15]	74	0.57	np-ZrO_2	ZrO_2	0.028
preceramic polymer	SiC [17]	40	0.52	Polycarbosilane (PCS)	SiC	0.218
	SiC [18]	16	0.44	Polycarbosiloxane (PCSO)	SiOC	0.409

Importantly, the initial relative density values reported in different studies on reactive binders are not directly comparable: in some instances initial relative density was reported as the relative density prior to reactive binder treatment [13, 22], while in other reports it was the relative density after reactive binder treatment [11, 14]. To compare the efficacy of these different reactive binders, we compensate for the different descriptions of initial relative density by defining the initial relative density as that of the powder aggregate prior to reactive binder treatment. To estimate initial relative density for systems without published data, we use results from Yang et al. [49] which give initial relative density as a function of particle diameter *d*. These results are summarized in **Figure 15**, constructed using data from **Figure 4** in Ref. 46. This calibration curve was used with the reported particle size in the different reactive binder studies to calculate ρ_0 values in **Table 1**.

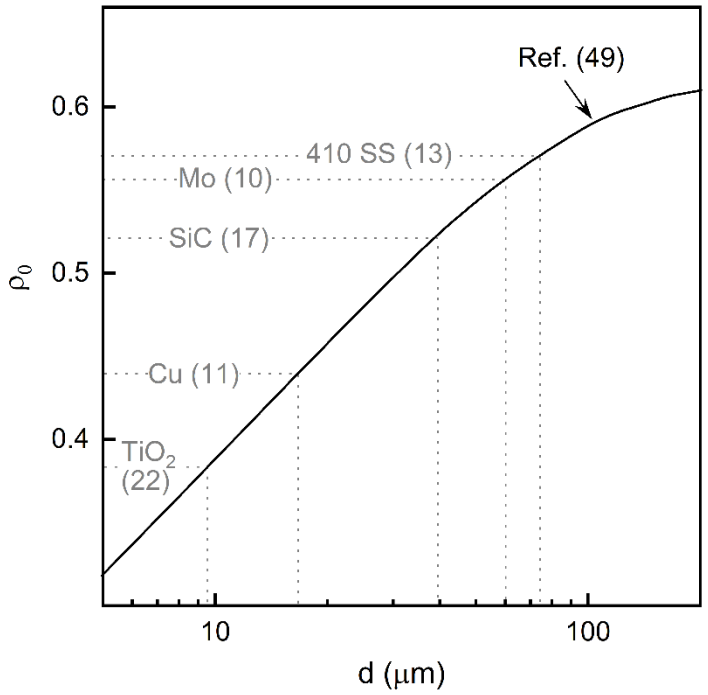

Figure 15: Initial relative density ρ_0 as a function of particle size d for respective reports calculated using results from simulations by Yang et al. (solid line) [49]

Here, we examine the effects of initial relative density and volume fraction yield ϕ of the reactive binder on the relative density ρ, coordination number Z, normalized area of a single contact $\bar{a} = a/4\pi R^2$, and fractional contact area $A_f = Za/4\pi R^2$. These parameters can be combined with **Equations 4**, **9**, and **13** to predict the average contact stress, effective viscosity, and sintering stress exhibited by a sintering compact treated with a given reactive binder.

Figure 16a shows iso-contours of relative density from a single reactive binder treatment, calculated using **Equation 16**. Reactive binders based on similar chemistries form clusters because they have similar solid yield. Preceramic polymers have the highest yield, on the order of 0.1, which is at least an order of magnitude higher than the yield of nanoparticle suspensions [13-15], where there are issues with agglomeration, and of soluble metal compounds [10, 11, 22], where low solubilities limit yield to 10^{-3}–10^{-2}. The maximum

increment in relative density ($\Delta\rho = \rho - \rho_0$) is observed for the preceramic polymer polycarbosiloxane (PCSO), for which $\Delta\rho = 0.2$. The increment in relative density for the nanoparticle suspensions and soluble metal compounds both range between 10^{-2} and 10^{-3}. The three datapoints at $\rho_0 = 0.44$ for Cu/metal-organic ink, Cu/np-Cu, and SiC/PCSO are representative of each class of reactive binder and highlight the differences in $\Delta\rho$ between each, signifying the importance of yield on final relative density. The reduction in the average contact stress from a single reactive binder treatment can be predicted by combining ρ and ρ_0 from **Figure 16a** with **Equation 4**.

Figure 16b shows iso-contours of constant coordination number Z calculated from **Equation 15**. The powder aggregates in the reports summarized here all have an initial average coordination number of 4 to 5. This coordination number is typical for loosely packed compacts but is lower than the average coordination number of Z = 7 in random close packed compacts with $\rho_0 = 0.64$. The negative curvature of the iso-contours means that a large yield is required to increase the average coordination number. The maximum increment in coordination number ($\Delta Z = Z - Z_0$) is observed for the preceramic polymer PCSO, with $\Delta Z = 2$. Increasing the initial packing density has a more significant effect on increasing Z than solely relying on reactive binder yield. This is especially true when using soluble metal compounds and nanoparticle suspensions, for which the yield is typically less than 0.1 and results in a ΔZ less than unity.

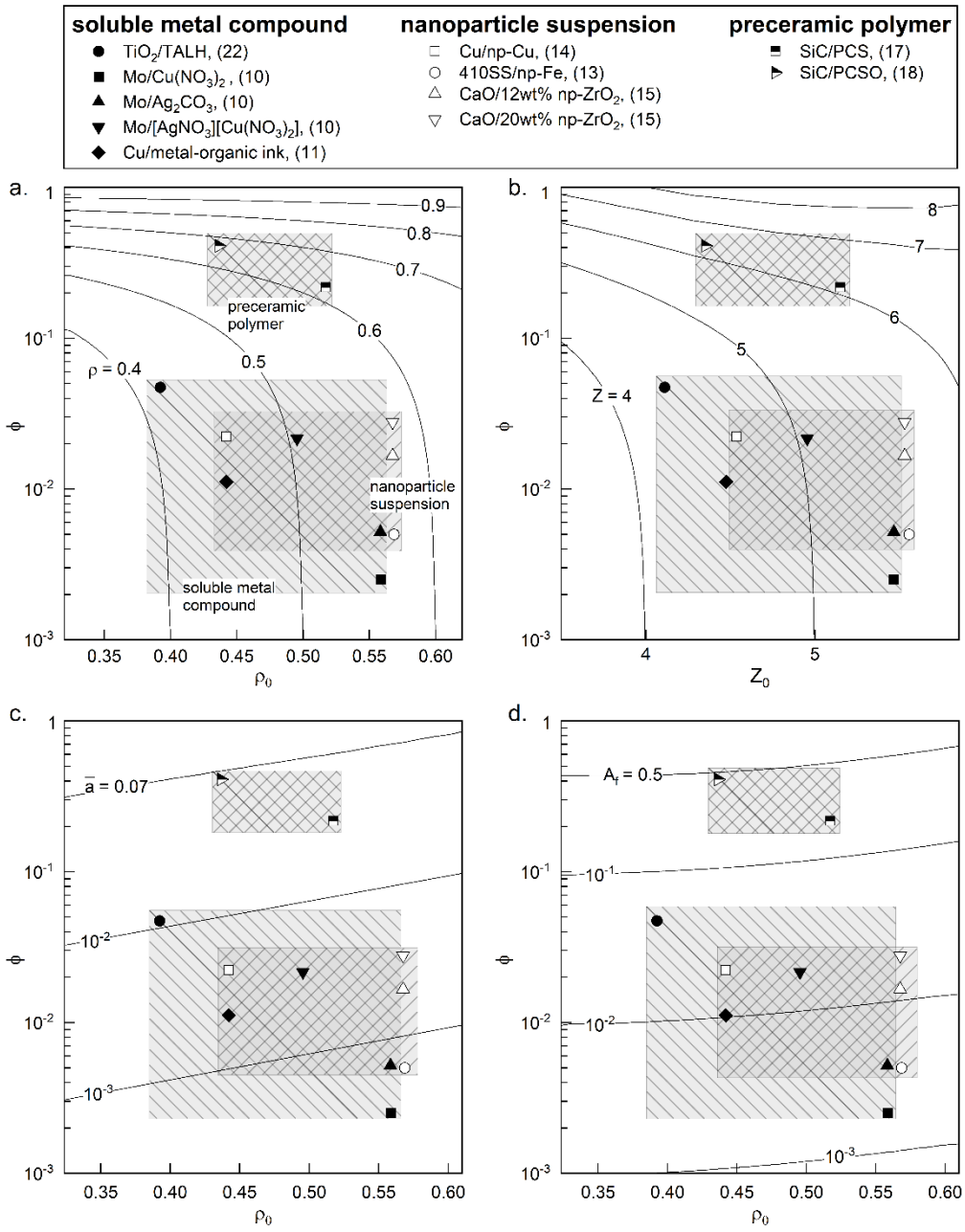

Figure 16: Reactive binder comparisons. The effect of volumetric yield and initial relative density on the (a) relative density, (b) coordination number, (c) area of a single contact, and (d) total fractional contact area

In addition to increasing the coordination number, reactive binder treatment increases the size of existing contacts. **Figure 16c** shows iso-contours of normalized contact area $\bar{a} = a/4\pi R^2$. When comparing the different material systems, the preceramic polymers have $\bar{a}$ on the order of 10^{-2}, while the nanoparticle and soluble metal compounds have $\bar{a}$ ranging

from 10^{-4}–10^{-2}, further emphasizing the benefit of a high yield for increasing contact area. Note that the positive slope of the $\bar{a}$ iso-contours is because the low average coordination number at low relative densities results in more material deposited at each interparticle neck than in more dense compacts. The effect of coordination number on the increment in contact size can be seen when comparing the data points at ϕ = 0.02; here, the coordination number for CaO/20wt% np-ZrO_2 (Z = 5.5) is greater than the coordination number for Cu/np-Cu (Z = 4.5). Consequently, CaO/20wt% np-ZrO_2 has a smaller contact area ($\bar{a}$ = 0.003) than Cu/np-Cu ($\bar{a}$ = 0.005).

Figure 16d is shown with iso-contours given by the product of Z and $\bar{a}$. Using the same comparison from earlier, the A_f of CaO/20wt% np-ZrO_2 is comparable to that for Cu/np-Cu (A_f = 0.02). The fractional contact area plotted in **Figure 16d** can be combined with **Equation 9** to predict the uniaxial viscosity of the sintering compacts. Note that the homogeneous TiO_2/TALH-derived TiO_2 system presented in this work leads to the same effective diffusivity term for both treated and untreated material. However, the versatility the reactive binder and feedstock powder combinations introduces the ability to tailor the diffusion kinetics as well (e.g., using sintering aids [9, 50] that promote densification while simultaneously increasing the fractional contact area).

In summary, **Figure 16** shows the effect of initial relative density and reactive binder yield on the size and quantity of the interparticle contacts. Increasing initial relative density increases the number of interparticle contacts but does not significantly affect the contact size. In contrast, increasing yield results in larger neck sizes with little effect on the coordination number. From **Equations 4** and **5**, this increase in neck size from the reactive binder treatment decreases contact stresses and the extent of creep. However, when

considering the effect of reactive binder treatment on the pore curvature, this specific deposition method can reduce the driving force for sintering, presenting a tradeoff between increasing effective viscosity and promoting densification driven by local gradients in surface curvature at interparticle necks.

7. Conclusions

We have quantified the mechanisms by which the reactive binder TALH affects the sintering mechanics in sintering binder jet printed TiO_2 compacts through a combination of structural characterization, loading dilatometry experiments, and micromechanics modeling. The key insights from this work include the following:

- TALH-treated material exhibits lower creep and densification strains than untreated material sintered for the same amount of time. However, at equivalent relative density, the TALH-treated material exhibits faster creep and densification than the untreated material.
- The measured activation energy ($Q \sim 400\text{kJ/mol}$) and stress exponent ($n \sim 1$) indicate that both the TALH-treated and untreated materials deform via lattice-mediated diffusional creep.
- The constitutive creep model reveals that the dominant effect of TALH on the sintering mechanics is to increase the interparticle contact size prior to sintering. However, due to differences in material distribution between TALH treatment and sintering, the average contact area in untreated specimens is 5-10% larger than in TALH-treated material sintered to the same relative density. This results in a lower uniaxial viscosity in TALH-treated compacts and a lower sintering stress, revealing lower surface curvature in the same.

- A survey of reactive binder and powder agglomerate combinations available in the open literature revealed that the reactive binder volume yield is a key variable for controlling the fractional contact area prior to sintering. When comparing soluble metal compounds, nanoparticle suspensions, and preceramic polymers, preceramic polymers, with a yield of 80%, increase the fractional contact area the most, indicating an excellent ability to decrease contact stresses, and increase the effective viscosity of the material prior to sintering.

Acknowledgements: We gratefully acknowledge Dr. Isha Gupta for her helpful insights on the sintering mechanics and Dr. Reid Carazzone for discussions on sintering. The authors gratefully acknowledge support from the NSF through project number NSF-CMMI-1826064. LOG also acknowledges support from the Ford Predoctoral Fellowship and the NSF Graduate Research Fellowship Program under Grant No. 1842494. The authors would also like to thank Saint-Gobain Ceramics & Plastics Inc., for donating the TiO_2 powder used in the project.

References

[1] M. Ziaee, N.B. Crane, Binder jetting: A review of process, materials, and methods, Addit Manuf. 28 (2019) 781-801. doi: 10.1016/j.addma.2019.05.031

[2] A. Mostafaei, A.M. Elliott, J.E. Barnes, F. Li, W. Tan, C.L. Cramer, P. Nandwana, M. Chmielus, Binder jet 3D printing—Process parameters, materials, properties, modeling, and challenges, Prog. Mater Sci. 119 (2021) 100707. doi: 10.1016/j.pmatsci.2020.100707

[3] A. Mostafaei, P. Rodriguez De Vecchis, I. Nettleship, M. Chmielus, Effect of powder size distribution on densification and microstructural evolution of binder-jet 3D-printed alloy 625, Mater. Des. 162 (2019) 375-383. doi: 10.1016/j.matdes.2018.11.051

[4] M.N. Rahaman, L.C. Jonghe, R.J. Brook, Effect of Shear Stress on Sintering, J. Am. Ceram. Soc. 69(1) (1986) 53-58. doi: 10.1111/j.1151-2916.1986.tb04693.x

[5] E. Sachs, S. Allen, H. Guo, J. Banos, M. Cima, J. Serdy, D. Brancazio, Progress on Tooling by 3D Printing; Conformal Cooling, Dimensional Control, Surface Finish and Hardness, Solid Freeform Fabr. Symp. Proc., Austin, Texas, pp. 115-124.

[6] R. German, Sintering: From Empirical Observations to Scientific Principles, Butterworth-Heinemann, 2014. doi: 10.1016/C2012-0-00717-X

[7] E.M. Sachs, C. Hadjiloucas, S. Allen, H. Yoo, Metal and ceramic containing parts produced from powder using binders derived from salt, Massachusetts Institute of Technology.

[8] F.F. Lange, Powder Processing Science and Technology for Increased Reliability, J. Am. Ceram. Soc. 72(1) (1989) 3-15. doi: 10.1111/j.1151-2916.1989.tb05945.x

[9] D. Oropeza, A.J. Hart, Reactive binder jet additive manufacturing for microstructural control and dimensional stability of ceramic materials, Addit Manuf. (2021) 102448. doi: 10.1016/j.addma.2021.102448

[10] E. Sachs, S. Allen, C. Hadjiloucas, J. Yoo, M. Cima, Low Shrinkage Metal Skeletons by Three Dimensional Printing, Solid Freeform Fabr. Symp. Proc., Austin, Texas, pp. 411-426.

[11] Y. Bai, C.B. Williams, Binder jetting additive manufacturing with a particle-free metal ink as a binder precursor, Mater. Des. 147 (2018) 146-156. doi: 10.1016/j.matdes.2018.03.027

[12] W. Du, X. Ren, C. Ma, Z. Pei, Ceramic binder jetting additive manufacturing: Particle coating for increasing powder sinterability and part strength, Mater. Lett. 234 (2019) 327-330. doi: 10.1016/j.matlet.2018.09.118

[13] N.B. Crane, J. Wilkes, E. Sachs, S.M. Allen, Improving accuracy of powder sintering-based SFF processes by metal deposition from nanoparticle dispersion, Solid Freeform Fabr. Symp. Proc., Austin, Texas, pp. 261-272.

[14] Y. Bai, C.B. Williams, Binderless Jetting: Additive Manufacturing of metal parts via jetting nanoparticles, Solid Freeform Fabr. Symp. Proc., Austin, Texas, pp. 249-260.

[15] H. Zhao, C. Ye, S. Xiong, Z. Fan, L. Zhao, Fabricating an effective calcium zirconate layer over the calcia grains via binder-jet 3D-printing for improving the properties of calcia ceramic cores, Addit Manuf. 32 (2020) 101025. doi: 10.1016/j.addma.2019.101025

[16] M. Singh, M.C. Halbig, J.E. Grady, Additive Manufacturing of Light Weight Ceramic Matrix Composites for Gas Turbine Engine Applications, John Wiley & Sons, 2016. doi: 10.1002/9781119211662.ch16

[17] I. Polozov, N. Razumov, D. Masaylo, A. Silin, Y. Lebedeva, A. Popovich, Fabrication of Silicon Carbide Fiber-Reinforced Silicon Carbide Matrix Composites Using Binder Jetting Additive Manufacturing from Irregularly-Shaped and Spherical Powders, Materials 13(7) (2020) 1766. doi: 10.3390/ma13071766

[18] C.L. Cramer, H. Armstrong, A. Flores-Betancourt, L. Han, A.M. Elliott, E. Lara-Curzio, T. Saito, K. Nawaz, Processing and properties of SiC composites made via binder jet 3D printing and infiltration and pyrolysis of preceramic polymer, Int. J. Ceram. Eng. Sci. 2(6) (2020) 320-331. doi: 10.1002/ces2.10070

[19] A. Zocca, H. Elsayed, E. Bernardo, C.M. Gomes, M.A. Lopez-Heredia, C. Knabe, P. Colombo, J. Günster, 3D-printed silicate porous bioceramics using a non-sacrificial preceramic polymer binder, Biofabrication 7(2) (2015) 025008. doi: 10.1088/1758-5090/7/2/025008

[20] K. Terrani, B. Jolly, M. Trammell, 3D printing of high-purity silicon carbide, J. Am. Ceram. Soc. 103(3) (2020) 1575-1581. doi: 10.1111/jace.16888

[21] M. Salehi, S. Maleksaeedi, S.M.L. Nai, G.K. Meenashisundaram, M.H. Goh, M. Gupta, A paradigm shift towards compositionally zero-sum binderless 3D printing of magnesium alloys via capillary-mediated bridging, Acta Mater. 165 (2019) 294-306. doi: 10.1016/j.actamat.2018.11.061

[22] L.O. Grant, M.B. Alameen, J.R. Carazzone, C.F. Higgs III, Z.C. Cordero, Mitigating Distortion During Sintering Of Binder Jet Printed Ceramics, Solid Freeform Fabr. Symp. Proc., Austin, Texas, 2018.

[23] M.N. Rahaman, L.C. Jonghe, M.-Y. Chu, Effect of Green Density on Densification and Creep During Sintering, J. Am. Ceram. Soc. 74(3) (1991) 514-519. doi: 10.1111/j.1151-2916.1991.tb04053.x

[24] F.B. Swinkels, M.F. Ashby, A second report on sintering diagrams, Acta Metall. 29(2) (1981) 259-281. doi: 10.1016/0001-6160(81)90154-1

[25] Q.D. Truong, L.X. Dien, D.-V.N. Vo, T.S. Le, Controlled synthesis of titania using water-soluble titanium complexes: A review, Journal of Solid State Chemistry 251 (2017) 143-163. doi: 10.1016/j.jssc.2017.04.017

[26] R. Lupitskyy, V.K. Vendra, J. Jasinski, D.A. Amos, M.K. Sunkara, T. Druffel, Toward high-efficiency dye-sensitized solar cells with a photoanode fabricated via a simple water-based formulation: Toward simple high-efficiency dye sensitized solar cells, Progress in Photovoltaics: Research and Applications 23(7) (2015) 883-891. doi: 10.1002/pip.2502

[27] R. Raj, Separation of Cavitation-Strain and Creep-Strain During Deformation, J. Am. Ceram. Soc. 65(3) (1982) C-46. doi: 10.1111/j.1151-2916.1982.tb10397.x

[28] H.U. Anderson, Initial Sintering of Rutile, J. Am. Ceram. Soc. 50(5) (1967) 235-238. doi: 10.1111/j.1151-2916.1967.tb15094.x

[29] R.D. Carnahan, J.O. Brittain, Optical Absorption Study of the Reduction Kinetics of Rutile Crystals, J. Am. Ceram. Soc. 48(7) (1965) 365-369. doi: 10.1111/j.1151-2916.1965.tb14762.x

[30] S. Pejovnik, D. Sušnik, D. Kolar, Densification of TiO_2 by hot pressing, Ceramurgia Int. 3(3) (1977) 92-94. doi: 10.1016/0390-5519(77)90002-3

[31] P. Kofstad, Nonstoichiometry, diffusion, and electrical conductivity in binary metal oxides, John Wiley & Sons, 1972. doi: 10.1002/maco.19740251027

[32] A.S. Helle, K.E. Easterling, M.F. Ashby, Hot-isostatic pressing diagrams: New developments, Acta Metall. 33(12) (1985) 2163-2174. doi: 10.1016/0001-6160(85)90177-4

[33] R.K. Bordia, G.W. Scherer, On constrained sintering—I. Constitutive model for a sintering body, Acta Metall. 36(9) (1988) 2393-2397. doi: 10.1016/0001-6160(88)90189-7

[34] R. Zuo, E. Aulbach, J. Rödel, Experimental determination of sintering stresses and sintering viscosities, Acta Mater. 51(15) (2003) 4563-4574. doi: 10.1016/S1359-6454(03)00293-3

[35] R.M. McMeeking, L.T. Kuhn, A diffusional creep law for powder compacts, Acta Metall. Mater. 40(5) (1992) 961-969. doi: 10.1016/0956-7151(92)90073-N

[36] M. Cologna, V.M. Sglavo, Vertical sintering to measure the uniaxial viscosity of thin ceramic layers, Acta Mater. 58(17) (2010) 5558-5564. doi: 10.1016/j.actamat.2010.06.007

[37] S.E. Schoenberg, D.J. Green, G.L. Messing, Effect of Green Density on the Thermomechanical Properties of a Ceramic During Sintering, J. Am. Ceram. Soc. 89(8) (2006) 2448-2452. doi: 10.1111/j.1551-2916.2006.01097.x

[38] R. Zuo, E. Aulbach, J. Rödel, Viscous Poisson's coefficient determined by discontinuous hot forging, J. Mater. Res. 18(9) (2003) 2170-2176. doi: 10.1557/JMR.2003.0303

[39] R.K. Bordia, G.W. Scherer, On constrained sintering—II. Comparison of constitutive models, Acta Metall. 36(9) (1988) 2399-2409. doi: 10.1016/0001-6160(88)90190-3

[40] C. Cao, R. Mücke, F. Wakai, O. Guillon, Viscous Poisson's ratio, bulk and shear viscosity during electrical field assisted sintering of polycrystalline ceria, Scripta Materialia 178 (2020) 240-243. doi: 10.1016/j.scriptamat.2019.11.043

[41] K.R. Venkatachari, R. Raj, Shear Deformation and Densification of Powder Compacts, J. Am. Ceram. Soc. 69(6) (1986) 499-506. doi: 10.1111/j.1151-2916.1986.tb07452.x

[42] E. Arzt, The influence of an increasing particle coordination on the densification of spherical powders, Acta Metall. 30(10) (1982) 1883-1890. doi: 10.1016/0001-6160(82)90028-1

[43] R.A. Gregg, F.N. Rhines, Surface tension and the sintering force in copper, Metall. Trans. 4(5) (1973) 1365-1374. doi: 10.1007/BF02644534

[44] R.k. Bordia, R. Raj, Sintering Behavior of Ceramic Films Constrained by a Rigid Substrate, J. Am. Ceram. Soc. 68(6) (1985) 287-292. doi: 10.1111/j.1151-2916.1985.tb15227.x

[45] C. Herring, Surface Tension as a Motivation for Sintering, in: J.M. Ball, D. Kinderlehrer, P. Podio-Guidugli, M. Slemrod (Eds.), Fundamental Contributions to the Continuum Theory of Evolving Phase Interfaces in Solids, Springer Berlin Heidelberg1999, pp. 33-69. doi: 10.1007/978-3-642-59938-5_2

[46] W.S. Coblenz, J.M. Dynys, R.M. Cannon, R.L. Coble, Initial stage solid state sintering models - A critical analysis and assessment, Mater. Sci. Res. 13 (1980) 141-157. doi: 10.1007/978-1-4899-5301-8_12

[47] G.D. Scott, Radial distribution of the random close packing of equal spheres, Nature 194 (1962) 956-957. doi: 10.1038/194956a0

[48] G. Mason, Radial Distribution Functions from Small Packings of Spheres, Nature 217(5130) (1968) 733-735. doi: 10.1038/217733a0

[49] R.Y. Yang, R.P. Zou, A.B. Yu, Computer simulation of the packing of fine particles, Phys. Rev. E 62(3) (2000) 3900-3908. doi: 10.1103/PhysRevE.62.3900

[50] J. Nie, J.M. Chan, M. Qin, N. Zhou, J. Luo, Liquid-like grain boundary complexion and sub-eutectic activated sintering in CuO-doped TiO_2, Acta Mater. 130 (2017) 329-338. doi: 10.1016/j.actamat.2017.03.037

[51] R.S. Averback, H.J. Höfler, H. Hahn, J.C. Logas, Sintering and grain growth in nanocrystalline ceramics, Nanostructured Materials 1(2) (1992) 173-178. doi: 10.1016/0965-9773(92)90072-6

[52] J.C. Alexander, Appendix A Defect Chemistry of TiO_2, Surface Modifications and Growth of Titanium Dioxide for Photo-Electrochemical Water Splitting, Springer International Publishing2016, pp. 303-311. doi: 10.1007/978-3-319-34229_0

[53] H.J. Frost, M.F. Ashby, Deformation-Mechanism Maps, The Plasticity and Creep of Metals and Ceramics Pergamon Press, 1982.

[54] C. Herring, Diffusional Viscosity of a Polycrystalline Solid, Journal of Applied Physics 21(5) (1950) 437-445. doi: 10.1063/1.1699681

[55] M.R. Notis, Deformation Mechanism Maps — A Review with Applications, in: R.C. Bradt, R.E. Tressler (Eds.), Deformation of Ceramic Materials, Springer US, Boston, MA, 1975, pp. 1-23. doi: 10.1007/978-1-4613-4431-5_1

[56] R.L. Coble, A Model for Boundary Diffusion Controlled Creep in Polycrystalline Materials, Journal of Applied Physics 34(6) (1963) 1679-1682. doi: 10.1063/1.1702656

[57] R. Raj, M.F. Ashby, On grain boundary sliding and diffusional creep, Metall. Trans. 2(4) (1971) 1113-1127. doi: 10.1007/BF02664244

[58] W.M. Hirthe, J.O. Brittain, High-Temperature Steady-State Creep in Rutile, J. Am. Ceram. Soc. 46(9) (1963) 411-417. doi: 10.1111/j.1151-2916.1963.tb11767.x

[59] D.G. Isaak, J.D. Carnes, O.L. Anderson, H. Cynn, E. Hake, Elasticity of TiO_2 rutile to 1800 K, Phys. Chem. Miner. 26(1) (1998) 31-43. doi: 10.1007/s002690050158

[60] D.A. Venkatu, Discussion of "Compressive Creep of Rutile at High Temperatures", J. Am. Ceram. Soc. 55(1) (1972) 258-262. doi: 10.1111/j.1151-2916.1972.tb13409.x

[61] J.E. Epperson, R.W. Siegel, J.W. White, T.E. Klippert, A. Narayanasamy, J.A. Eastman, F. Trouw, Sintering of Nanophase TiO_2 at 550°C, MRS Proceedings 132 (1988) 15-20. doi: 10.1557/PROC-132-15

Appendix A. Grain growth in TALH-derived TiO_2

Our previous work showed that TALH-derived TiO_2 heated to 900 °C is predominantly rutile and has an average grain size of 150 nm [22]. Thus grain growth of the TALH-derived TiO_2 can be approximated following a grain growth expression for nanocrystalline TiO_2 developed by Höfler and Averback [51]:

$$D^3 = D_0^3 + \alpha \exp\left(\frac{-Q}{RT}\right) t^n, \quad \text{(A1)}$$

where D_0 is the initial grain size, α is the grain boundary preexponent ($\alpha = 7.29 \times 10^{-10}$ m^3/s) [51], n is a time exponent ($n \approx 1$ for T = 700–825 °C) [51], and Q_b is an activation energy for grain boundary diffusion (Q_b = 278 kJ/mol) [51]. As shown in **Figure A1**, Eq A1 predicts that the average grain size of the TALH-derived TiO_2 grows to ~10 μm within 40 minutes when heating at a rate of 12 K/min. Note that this is essentially the same as the particle size of the powder feedstock.

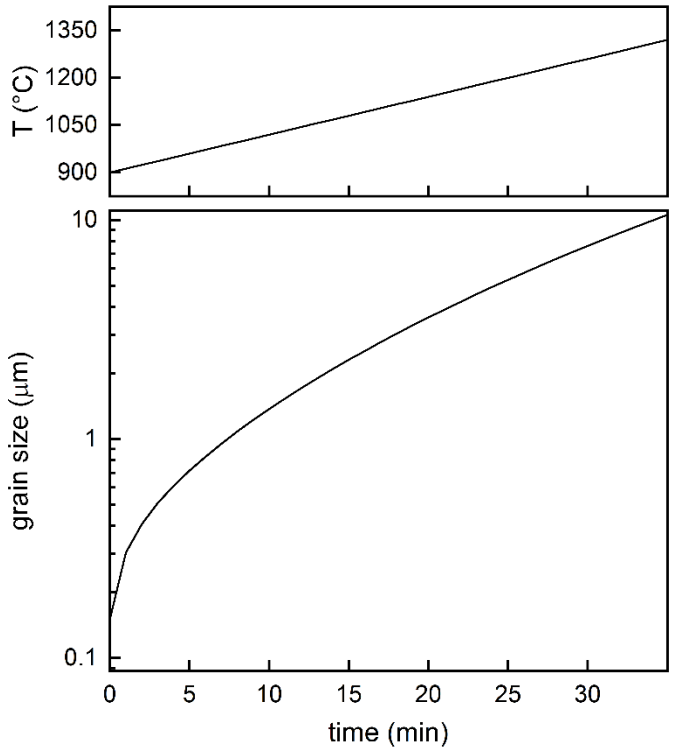

Figure A1: Predicted grain size of the TALH-derived material as a function of time for the sintering cycle used in the present study.

Appendix B. Activation energy for lattice diffusion in rutile TiO_2

The most common intrinsic point defects in TiO_2 include oxygen vacancies and titanium interstitial cations (Ti^{3+}, Ti^{4+}) [31], with oxygen vacancies dominating under the sintering conditions used in the present work (~1 atm O_2; 1100–1500 °C). Under these conditions, the concentration of oxygen vacancies is given by [52]

$$[V_{\ddot{O}}] = \left[K_0 \exp\left(\frac{\Delta S_{V_{\ddot{O}}}}{k}\right) \exp\left(\frac{-\Delta H_{V_{\ddot{O}}}}{kT}\right)\right]^{\frac{1}{3}} \quad \text{(B1)}$$

where T is the absolute temperature, k is Boltzmann's constant, K_0 is equilibrium constant (which is a function of oxygen partial pressure for non-stoichiometric rutile TiO_2), and $\Delta S_{V_{\ddot{O}}}$ and $\Delta H_{V_{\ddot{O}}}$ are, respectively, the entropy and enthalpy of oxygen vacancy formation. Multiplying this expression by the oxygen vacancy mobility:

$$D = D_0 \exp\left(\frac{\Delta S_m}{k}\right) \exp\left(\frac{-\Delta H_m}{kT}\right) \quad \text{(B2)}$$

where D_0 diffusion preexponent and ΔS_m and ΔH_m are the entropy and enthalpy for migration, gives the intrinsic oxygen vacancy diffusivity, for which the total activation energy Q is[31]

$$Q = \frac{\Delta H_{V_{\ddot{o}}}}{3} + \Delta H_m. \quad \text{(B3)}$$

The enthalpy of formation of oxygen vacancies is $H_{V_{\ddot{o}}} = 439$ kJ/mol [31] and the enthalpy of vacancy migration *is* H_m = 250 kJ/mol [28, 31], giving Q = 396 kJ/mol, in excellent agreement with our experimental measurement of Q ≈ 400 kJ/mol. This result supports that the TALH-treated and neat materials creep by lattice diffusion of oxygen vacancies and that extrinsic point defects are not significant.

Appendix C. Constructing the deformation mechanism map

The deformation mechanism map in **Figure 9** was constructed following the approach described by Frost and Ashby [53]. We consider three main creep mechanisms: Nabarro-Herring creep characterized by lattice diffusion of point defects; Coble creep characterized by grain boundary diffusion; and power-law creep characterized by dislocation climb and glide. Each mechanism contributes a unique creep strain rate under a given combination of applied stress and temperature. Deformation mechanism maps indicate regions in normalized stress-temperature space where a given mechanism has the fastest creep rate.

We use standard expressions to compute the creep rates for the different mechanisms. The rate equation for Nabarro-Herring creep [54, 55] is

$$\dot{\varepsilon}_{\mathrm{NH}} = \frac{13.3\, D_v \Omega \sigma}{kT d^2}, \quad \text{(C1)}$$

where D_v is the lattice diffusivity expressed as $D_v = D_{0v}\exp(-Q_v/RT)$, D_{0v} is the lattice diffusion preexponent, Q_v is the activation energy for lattice diffusion, R is the ideal gas constant, Ω is the atomic volume, σ is the applied shear stress, k is Boltzmann's constant, T is the temperature and d is the grain size. The rate equation for Coble creep [55, 56] is

$$\dot{\varepsilon}_C = \frac{47.5\,\delta D_b \Omega \sigma}{kTd^3} \tag{C2}$$

where D_b is the grain boundary diffusivity expressed as $D_b = D_{0b}\exp(-Q_b/RT)$, D_b is the grain boundary preexponent, Q_b is the activation energy for grain boundary diffusion, and δ is the grain boundary thickness. The rate equation for power law creep [55, 57] is

$$\dot{\varepsilon}_{PL} = A\frac{D_v \mu b}{kT}\left(\frac{\sigma}{\mu}\right)^n, \tag{C3}$$

where A is the Dorn parameter, and μ is the temperature-dependent shear modulus given by

$$\mu = \mu_0\left[1 + \frac{(T-300)}{T_m}\,\frac{T_m}{\mu_0}\frac{d\mu}{dT}\right], \tag{C4}$$

where μ_0 is the shear modulus at 300 K, $(d\mu/dT)$ is the rate of change of shear modulus with temperature, and T_m is the melting temperature. The material property data used to construct the deformation mechanism map for rutile TiO_2 is listed in **Table C1**.

Table C1. Material property data used to construct deformation mechanism map

material property	value
atomic volume, Ω (Å^3)	31 [30]
Burger's vector, b (Å)	3 [30],[58]
melting temperature, T_m (K)	2112 [30],[58]
shear modulus at 300 K, μ_0 (GPa)	113 [58]
temperature dependance of modulus, $\frac{d\mu}{dT}$ (GPa/K)	-0.34 [59]
lattice preexponent, D_{0v} (m^2/sec)	3.50x10^{-6} [30]
lattice activation energy, Q_v (kJ/mol)	251 [30],[60]
grain boundary width, δ (nm)	0.5 [61]
grain boundary preexponent, D_{0b} (μm/s)	7 [30]
grain boundary activation energy, Q_b (kJ/mol)	200 [30]
stress exponent, n	3 [30]
dorn Parameter, A	3 [30]
particle size, d (μm)	9